A multifractal formalism for vector-valued random fields based on wavelet analysis: application to turbulent velocity and vorticity 3D numerical data

Pierre Kestener[1,2] and Alain Arneodo[2,3]

[1]CEA-Saclay, DSM/DAPNIA/SEDI, 91191 Gif-sur-Yvette, France

[2]Laboratoire de Physique, Ecole Normale Supérieure de Lyon, 46 allée d'Italie, 69364 Lyon cédex 07, France

[3]Laboratoire Transdisciplinaire Joliot Curie, Ecole Normale Supérieure de Lyon, 46 allée d'Italie, 69364 Lyon cédex 07, France

(Dated: February 27, 2007)

Extreme atmospheric events are intimately related to the statistics of atmospheric turbulent velocities. These, in turn, exhibit multifractal scaling, which is determining the nature of the asymptotic behavior of velocities, and whose parameter evaluation is therefore of great interest currently. We combine singular value decomposition techniques and wavelet transform analysis to generalize the multifractal formalism to vector-valued random fields. The so-called Tensorial Wavelet Transform Modulus Maxima (TWTMM) method is calibrated on synthetic self-similar 2D vector-valued multifractal measures and monofractal 3D vector-valued fractional Brownian fields. We report the results of some application of the TWTMM method to turbulent velocity and vorticity fields generated by Direct Numerical Simulations (DNS) of the incompressible Navier-Stokes equations. This study reveals the existence of an intimate relationship $D_{\boldsymbol{v}}(h+1) = D_{\boldsymbol{\omega}}(h)$, between the singularity spectra of these two vector fields which are found significantly more intermittent than previously estimated from longitudinal and transverse velocity increment statistics.

PACS numbers: 47.53.+n, 02.50.Fz, 05.40-a, 47.27.Gs

I. INTRODUCTION

Several studies over the last decade have shown that atmospheric extremes are subject to multifractal scaling [1–6], a finding that is heuristically supported by the multifractality found in chaotic dynamical systems in general [7–9], and in turbulent flows in particular [10–13]. Estimating the asymptotic behavior resulting from the observed scaling laws relies in a fundamental manner on the correctness of the parameterization of the multifractal singularity spectra in the domain where statistics are robust. Box-counting and correlation algorithms were successfully adapted to resolve multifractal scaling for isotropic self-similar fractals by computation of the generalized fractal dimensions D_q [14–18]. As to self-affine fractals [19, 20], Parisi and Frisch [21] proposed, in the context of the analysis of fully developed turbulence velocity data, an alternative multifractal description based on the investigation of the scaling behavior of the so-called structure functions [22, 23]: $S_p(l) =< (\delta v_l)^p > \ \sim \ l^{\zeta_p}$ (p integer > 0), where $\delta v_l(x) = v(x+l) - v(x)$ is an increment of the recorded longitudinal velocity component over a distance l. Then, from the local scaling behavior of the velocity increments, $\delta v_l(x) \sim l^{h(x)}$, the $D(h)$ singularity spectrum is defined as the Hausdorff dimension of the set of points x where the local roughness (or Hölder) exponent $h(x)$ of v is h [21, 24–27]. In principle, $D(h)$ can be attained by Legendre transforming the structure function scaling exponents ζ_p [21, 26, 27]. Unfortunately, as noticed by Muzy *et al* [28], there are some fundamental drawbacks to the structure function method. Indeed, it generally fails to fully characterize the $D(h)$ singularity spectrum since only the strongest singularities of the function v itself (and not the singularities present in the derivatives of v) are a priori amenable to this analysis. Even though one can extend this study from integer to real positive p values by considering the increment absolute value $|\delta v_l|$, the structure functions generally do not exist for $p < 0$, which makes the decreasing right part of the $D(h)$ singularity spectrum inaccessible to this method. Moreover, singularities corresponding to $h > 1$, as well as regular behavior, bias the estimate of ζ_p [26–28].

In a previous work, Arneodo and collaborators [26–28] have shown that there exists a natural way of performing a unified multifractal analysis of both singular measures and multi-affine functions, which consists in using the continuous wavelet transform (WT) [29–33]. By using wavelets instead of boxes, one can take advantage of freedom in the choice of these "generalized oscillating boxes" to get rid of possible smooth behavior that might either mask singularities or perturb the estimation of their strength h. The other fundamental advantage of using wavelets is that the skeleton defined by the wavelet transform modulus maxima (WTMM) [34, 35], provides an adaptive space-scale partitioning from which one can extract the $D(h)$ singularity spectrum via the scaling exponents $\tau(q)$ (q real positive as well as negative) of some partition functions defined from the WT skeleton. The so-called WTMM method [26–28] therefore provides access to the entire $D(h)$ spectrum via the usual Legendre transform $D(h) = \min_q\big(qh - \tau(q)\big)$. We refer the reader to Refs. [36, 37] for rigorous mathematical results and to Ref. [38] for the theoretical treatment of random multifractal functions. Let us also note that from a fundamental point of view, the WTMM multifractal formalism has been revisited in Refs. [39, 40], in order to incorporate in this statistical "canonical" description (which

applies for cusp-like singularities only), the possible existence of oscillating singularities [35, 39, 41]. This new "grand canonical" description [39, 40] allows us to compute the singularity spectrum $D(h, \beta)$, which accounts for the statistical contribution of singularities of Hölder exponent h and oscillating exponent β (where β characterizes the local power law divergence of the instantaneous frequency).

Applications of the WTMM method to 1D signal have already provided insight into a wide variety of problems [42, 43], e.g., the validation of the log-normal cascade phenomenology of fully developed turbulence [44–48], the characterization and the understanding of long-range correlations in DNA sequences [49–52], the demonstration of the existence of a causal cascade of information from large to small scales in financial time series [53, 54], the use of the multifractal formalism to discriminate between healthy and sick heartbeat dynamics [55, 56], the discovery of a Fibonacci structural ordering in 1D cuts of diffusion limited aggregates (DLA) [57–60]. The canonical WTMM method has been further generalized from 1D to 2D with the specific goal to achieve multifractal analysis of rough surfaces with fractal dimensions D_F anywhere between 2 and 3 [61–64]. The 2D WTMM methodology has been successfully applied to characterize the intermittent nature of satellite images of the cloud structure [61–64], to perform a morphological analysis of the anisotropic structure of atomic hydrogen (H1) density in Galatic spiral arms [65] and to assist in the diagnosis in digitized mammograms [66]. We refer the reader to Ref. [67] for a review of the 2D WTMM methodology, from the theoretical concepts to experimental applications.

In a recent work [68, 69], we have further extended the canonical WTMM method to 3D analysis. After some convincing test applications to synthetic 3D monofractal Brownian fields and to 3D multifractal realizations of singular cascade measures as well as their random function counterpart obtained by fractional integration, we have applied the 3D WTMM method to dissipation and enstrophy 3D numerical data issued from Direct Numerical Simulations (DNS) of isotropic turbulence. The results so obtained have revealed that the multifractal spatial structure of both the dissipation and enstrophy fields are likely to be well described by a multiplicative cascade process that is definitely non-conservative. This contrasts with the conclusions of previous box-counting analysis [11, 13, 70–75] that failed to estimate correctly the corresponding multifractal spectra because of their intrinsic inability to master non-conservative singular cascade measures [68, 69]. To our knowledge, thus far, the multifractal description has been mainly devoted to scalar measures and functions. However, in physics as well as in other fundamental and applied sciences, fractals appear not only as deterministic or random scalar fields but also as vector-valued deterministic or random fields. In the spirit of a preliminary theoretical study of self similar vector-valued measures by Falconer and O'Neil [76], our objective here is to generalize the WTMM method to multi-dimensional vector valued fields with the specific goal to achieve the first comparative 3D vectorial multifractal analysis of numerical velocity and vorticity fields generated in $(256)^3$ DNS of the incompressible Navier-Stokes equations. The preliminary results of this study have been announced in a previous short communication [77].

The article is organized as follows. In Section II, we define the tensorial wavelet transform of a vector-valued field. Using singular value decomposition techniques [78], we show how to characterize the (Hölder) regularity of this vector field taking into account all its components, from the scale-space decomposition provided by the Tensorial Wavelet Transform Modulus Maxima (TWTMM) method which generalizes the WTMM method to the multifractal analysis of vector-valued fields. Section III is devoted to test applications of the TWTMM method to synthetic self-similar 2D vector-valued multifractal measures and to monofractal 3D vector-valued fractional Brownian fields. In Section IV, we report the results of the application of the TWTMM method to DNS turbulence data. The singularity spectra of the full 3D velocity and vorticity fields are computed and compared to previous estimates obtained from longitudinal and transverse velocity increments. We conclude with some perspectives in Section V.

II. A WAVELET-BASED MULTIFRACTAL FORMALISM FOR VECTOR-VALUED FIELDS

A. The tensorial wavelet transform

Let us note $\mathbf{V}(\mathbf{x} = (x_1, x_2, .., x_d))$, a vector-valued field with square integrable scalar components $V_j(\mathbf{x})$, $j = 1, 2, .., d$. Along the line of the multi-dimensional WTMM method [62–64, 67–69], let us define d analyzing wavelets $\psi_i(\mathbf{x})$ that are, respectively, the partial derivatives of a smoothing scalar function $\phi(\mathbf{x})$:

$$\psi_i(\mathbf{x} = (x_1, x_2, ..., x_d)) = \partial\phi(\mathbf{x} = (x_1, x_2, ..., x_d))/\partial x_i, \quad i = 1, 2, .., d. \tag{2.1}$$

We will assume that ϕ is well localized around $|\mathbf{x}| = 0$ and that it is an isotropic function that depends on $|\mathbf{x}|$ only. In this work, we will mainly use the Gaussian function:

$$\phi(\mathbf{x} = (x_1, x_2, ..., x_d)) = e^{-|\mathbf{x}|^2/2}. \tag{2.2}$$

For our specific 3D application to DNS data in Section IV, we will test the robustness of our estimates of the multifractal spectra when using alternatively the isotropic mexican hat:

$$\phi(\mathbf{x}) = (3 - \mathbf{x}^2)e^{-|\mathbf{x}|^2/2}. \tag{2.3}$$

This will correspond to use third-order analyzing wavelets $\psi_i(\mathbf{x})$ $(i = 1, 2, .., d)$ with their three first moments equal to zero instead of first order analyzing wavelets with one zero moment only.

The wavelet transform of $\mathbf{V}$ with respect to ψ_i $(i = 1, 2, .., d)$, at the point $\mathbf{b}$ and the scale a can be expressed in a tensorial form [77]:

$$\mathbb{T}_{\boldsymbol{\psi}}[\mathbf{V}](\mathbf{b}, a) = \begin{pmatrix} T_{\psi_1}[V_1] & T_{\psi_1}[V_2] & ... & T_{\psi_1}[V_d] \\ T_{\psi_2}[V_1] & T_{\psi_2}[V_2] & ... & T_{\psi_2}[V_d] \\ \vdots & \vdots & & \vdots \\ T_{\psi_d}[V_1] & T_{\psi_d}[V_2] & ... & T_{\psi_d}[V_d] \end{pmatrix}, \tag{2.4}$$

where

$$T_{\psi_i}[V_j](\mathbf{b}, a) = a^{-d} \int d^d\mathbf{x}\, \psi_i\big(a^{-1}(\mathbf{x} - \mathbf{b})\big) V_j(\mathbf{x}). \tag{2.5}$$

Let us point out that each column vector of the tensor in Eq. (2.4) is nothing but the 3D wavelet transform of the component V_j of the vector field $\mathbf{V}$ [68, 69]. This vector $\mathbf{T}_{\boldsymbol{\psi}}[V_j]$ defines the direction and the amplitude of the largest variation of the scalar component V_j at scale a. Our strategy will thus consist in defining some equivalent for the vector field $\mathbf{V}$ itself, i.e., in finding the direction that locally corresponds to the maximum amplitude variation of $\mathbf{V}$. To be more concrete, this requires to find the column vector $\mathbf{C}$ that maximizes the following norm:

$$||\mathbb{T}_{\boldsymbol{\psi}}[\mathbf{V}]|| = \sup_{\mathbf{C}\neq 0} \frac{|\mathbb{T}_{\boldsymbol{\psi}}[\mathbf{V}].\mathbf{C}|}{|\mathbf{C}|}, \tag{2.6}$$

where $|\mathbf{C}| = \sqrt{\sum_{i=1}^{d} C_i^2}$ is the Euclidean norm of $\mathbb{R}^d$ and . denotes the usual matrix product. This can be obtained from the singular value decomposition [77, 78] of the matrix $(T_{\psi_i}[V_j])$ (Eq. (2.4)):

$$\mathbb{T}_{\boldsymbol{\psi}}[\mathbf{V}] = \mathbb{G}\Sigma\mathbb{H}^T, \tag{2.7}$$

where $\mathbb{G}$ and $\mathbb{H}$ are orthogonal matrices ($\mathbb{G}^T\mathbb{G} = \mathbb{H}^T\mathbb{H} = \mathbb{I}_d$) and $\Sigma = diag(\sigma_1, \sigma_2, .., \sigma_d)$ with $\sigma_i \geq 0$, for $1 \leq i \leq d$. The columns of $\mathbb{G}$ and $\mathbb{H}$ are referred to as the left and right singular vectors respectively, and the singular values of $\mathbb{T}_{\boldsymbol{\psi}}[\mathbf{V}]$ are defined as the diagonal elements of Σ which are the non-negative square roots of the d eigenvalues of $\mathbb{T}_{\boldsymbol{\psi}}[\mathbf{V}]^T\mathbb{T}_{\boldsymbol{\psi}}[\mathbf{V}]$. Let us note that this decomposition is unique, up to some permutation of the σ_i's. The direction of the largest amplitude variation of $\mathbf{V}$, at point $\mathbf{b}$, when seen at scale a by the "wavelet transform microscope", is thus given by the eigenvector $\mathbf{G}_\rho(\mathbf{b}, a)$ associated to the spectral radius

$$\rho(\mathbf{b}, a) = \max_j \sigma_j(\mathbf{b}, a). \tag{2.8}$$

One is thus led to the analysis of the vector field:

$$\mathbf{T}_{\boldsymbol{\psi},\rho}[\mathbf{V}](\mathbf{b}, a) = \rho(\mathbf{b}, a)\mathbf{G}_\rho(\mathbf{b}, a), \tag{2.9}$$

whose modulus is nothing but the spectral radius

$$\mathcal{M}_{\boldsymbol{\psi}}(\mathbf{b}, a) = |\mathbf{T}_{\boldsymbol{\psi},\rho}[\mathbf{V}](\mathbf{b}, a)| = \rho(\mathbf{b}, a). \tag{2.10}$$

Thus from the scaling behavior of the spectral radius, one can characterize the local Hölder regularity of the vector field $\mathbf{V}$. Let $h_j(\mathbf{x}_0)$, $j = 1, 2, .., d$, be the Hölder exponents of the d components of $\mathbf{V}$ respectively [19, 26, 36, 37]. Provided the number n_{ψ_j} of zero moments of the analyzing wavelets ψ_j be larger than $h_j(\mathbf{x}_0)$ for $j = 1, 2, .., d$, then as proved in Refs. [68, 69], the wavelet transform of the component V_j with respect to ψ_i behaves as:

$$T_{\psi_i}[V_j](\mathbf{x}_0, a) = \int d^d\mathbf{x}\, \psi_i(\mathbf{x}) V_j(\mathbf{x}_0 + a\mathbf{x}) = a^{h_j(\mathbf{x}_0)} C_j \int d^d\mathbf{x}\, \psi_i(\mathbf{x})\, |\mathbf{x}|^{h_j(\mathbf{x}_0)}. \tag{2.11}$$

It is then straightforward to show that, in the limit $a \to 0^+$, the scaling behavior of the spectral radius is dominated by the smallest Hölder exponent:

$$\rho(\mathbf{x}_0, a) \sim a^{\min_j h_j(\mathbf{x}_0)}, \tag{2.12}$$

that we will call the Hölder exponent of $\mathbf{V}$ at the point $\mathbf{x}_0$.

B. The tensorial wavelet transform modulus maxima method

Very much like what has been done for the WTMM analysis of multi-dimensional scalar fields [62, 67–69], let us define, at a given scale a, the WTMM as the position $\mathbf{b}$ where the modulus $\mathcal{M}_{\boldsymbol{\psi}}[\mathbf{V}](\mathbf{b},a) = \rho(\mathbf{b},a)$ (Eq. (2.10)) is locally maximum along the direction of $\mathbf{G}_\rho(\mathbf{b},a)$ (Eq. (2.9)). These WTMM lie on connected $(d-1)$ hypersurfaces called *maxima hypersurfaces* (see Figs. 3 and 7). In theory, at each scale a, one only needs to record the position of the local maxima of $\mathcal{M}_{\boldsymbol{\psi}}$ (WTMMM) along the maxima hypersurfaces together with the value of $\mathcal{M}_{\boldsymbol{\psi}}[\mathbf{V}]$ and the direction of $\mathbf{G}_\rho$. These WTMMM are disposed along connected curves accross scales called *maxima lines* [62, 67–69] living in a $(d+1)$-space $(x_1, x_2, .., x_d, a)$. The WT *skeleton* is then defined as the set of maxima lines that converge to the $(x_1, x_2, .., x_d)$ hyperplane in the limit $a \to 0^+$ (see Fig. 3d). As originally demonstrated in Ref. [69, 77], the local Hölder regularity of $\mathbf{V}$, as characterized by $h(\mathbf{x}_0) = \min_j h_j(\mathbf{x}_0)$, can be estimated from the power-law behavior of $\mathcal{M}_{\boldsymbol{\psi}}[\mathbf{V}]$:

$$\mathcal{M}_{\boldsymbol{\psi}}[\mathbf{V}]\big(\mathcal{L}_{\mathbf{x}_0}(a)\big) \sim a^{h(\mathbf{x}_0)}, \tag{2.13}$$

along the maxima line $\mathcal{L}_{\mathbf{x}_0}(a)$ pointing to the point $\mathbf{x}_0$ in the limit $a \to 0^+$, provided $h(\mathbf{x}_0)$ be smaller than the number $n_{\boldsymbol{\psi}}$ $(= \min_j n_{\psi_j})$ of zero moments of the analyzing wavelet $\boldsymbol{\psi}$ [68, 69, 77].

As recalled in the introduction, the multifractal formalism aims at computing the singularity spectrum $D(h)$ of the considered field, here the vector-valued field $\mathbf{V}$:

$$D(h) = d_H\{\mathbf{x} \in \mathbb{R}, h(\mathbf{x}) = h\}. \tag{2.14}$$

$D(h)$ associates with any h, the Hausdorff dimension of S_h, the set of all point $\mathbf{x}_0 \in \mathbb{R}$, so that the Hölder exponent of $\mathbf{V}$ is h. Mapping the WTMM methodology developed for multidimensional scalar fields [62, 67–69], we use the space-scale partitioning given by the WT skeleton to define the following partition functions:

$$\mathcal{Z}(q,a) = \sum_{\mathcal{L}\in\mathcal{L}(a)} \left(\mathcal{M}_{\boldsymbol{\psi}}[\mathbf{V}](\mathbf{x},a)\right)^q \ , \tag{2.15}$$

where $q \in \mathbb{R}$ and $\mathcal{L}(a)$ is the set of maxima lines that exist at scale a in the WT skeleton. From a deep analogy that links the multifractal formalism to statistical thermodynamics [7–9, 11, 27], one can define the scaling exponents $\tau(q)$ from the power-law behavior of the partition functions:

$$\mathcal{Z}(q,a) \sim a^{\tau(q)} \ , \ a \to 0^+ \ , \tag{2.16}$$

where q and $\tau(q)$ play respectively the role of the inverse temperature and the free energy. The main result of the tensorial wavelet based multifractal formalism [77] is that in place of the energy and the entropy (i.e. the thermodynamical variables conjugated to q and τ), one has the Hölder exponent h (Eq. (2.13)) and the singularity spectrum $D(h)$ (Eq. (2.14)). This means that the $D(h)$ singularity spectrum of $\mathbf{V}$ can be determined from the Legendre transform of the partition function scaling exponents $\tau(q)$:

$$D(h) = \min_q (qh - \tau(q)). \tag{2.17}$$

From the properties of the Legendre transform, it is easy to convince oneself that *homogeneous* (monofractal) vector-valued fields that involve singularities of a unique Hölder exponent $h = \partial\tau/\partial q$, are characterized by a $\tau(q)$ spectrum which is a *linear* function of q. On the contrary, a *non-linear* $\tau(q)$ curve is the signature of nonhomogenous fields that display *multifractal* properties, in the sense that the Hölder exponent $h(\mathbf{x})$ is a fluctuating quantity that depends upon the spatial position $\mathbf{x}$ (in other words, the local roughness exponent is fluctuating from point to point).

From a practical point of view, one can avoid performing the Legendre transform by considering the quantities h and $D(h)$ as mean quantities defined in a canonical ensemble, i.e. with respect to their Boltzmann weights computed from the WTMMM [26, 27, 62, 67–69]:

$$W_{\boldsymbol{\psi}}[\mathbf{V}](q,\mathcal{L},a) = \frac{\left(\mathcal{M}_{\boldsymbol{\psi}}[\mathbf{V}](\mathbf{x},a)\right)^q}{\mathcal{Z}(q,a)} \ , \tag{2.18}$$

where $\mathcal{Z}(q,a)$ is the partition function defined in Eq. (2.15). Then one computes the expectation values:

$$h(q,a) = \sum_{\mathcal{L}\in\mathcal{L}(a)} \ln\left|\mathcal{M}_{\boldsymbol{\psi}}[\mathbf{V}](\mathbf{r},a)\right| \ W_{\boldsymbol{\psi}}[\mathbf{V}](q,\mathcal{L},a) \ , \tag{2.19}$$

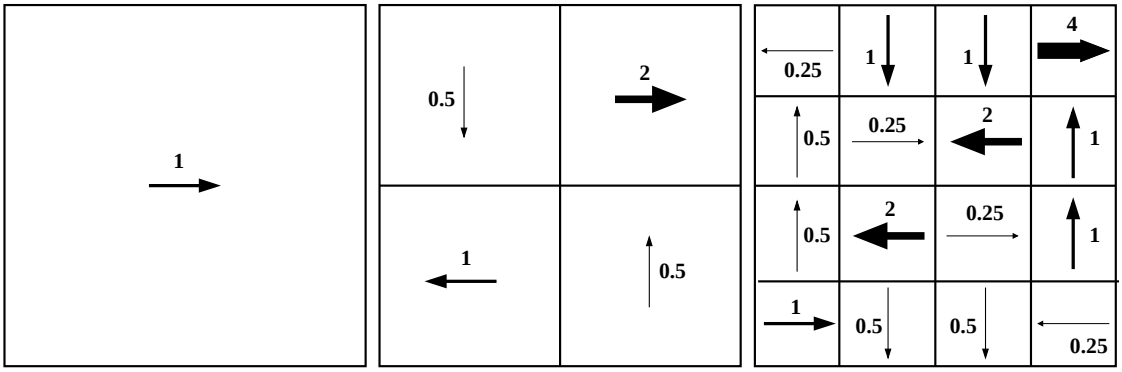

FIG. 1: First construction steps of a singular vector-valued measure supported by the unit square. The norm of the four similitudes S_i are $p_1 = p_4 = C = 1/2$, $p_2 = 2$ and $p_3 = 1$ [76].

and

$$D(q,a) = \sum_{\mathcal{L}\in\mathcal{L}(a)} W_{\boldsymbol{\psi}}[\mathbf{V}](q,\mathcal{L},a)\ \ln\big(W_{\boldsymbol{\psi}}[\mathbf{V}](q,\mathcal{L},a)\big)\ , \tag{2.20}$$

from which one extracts

$$h(q) = \lim_{a\to 0^+} h(q,a)/\ln a\ , \tag{2.21}$$

$$D(q) = \lim_{a\to 0^+} D(q,a)/\ln a\ , \tag{2.22}$$

and therefore the $D(h)$ singularity spectrum.

III. TEST APPLICATIONS OF THE TWTMM METHOD TO MONOFRACTAL AND MULTIFRACTAL SYNTHETIC VECTOR FIELDS

A. Multifractal vector-valued measures

As a first test application of the TWTMM method described in Section II to the vector situation, let us consider the self-similar vector measures defined on Euclidean space originally introduced by Falconer and O'Neil [76]. The σ-additivity property of positive scalar measures [7–9, 12, 19] is now replaced by the vectorial equality:

$$\boldsymbol{\mu}(\bigcup_{i=1}^{m} A_i) = \boldsymbol{\mu}(A_1) + ... + \boldsymbol{\mu}(A_m), \tag{3.1}$$

where $A_1, .., A_m$ are disjoint sets. In figure 1, are illustrated the first three steps in the construction of a multiplicative 2D vector measure supported by the unit square. From step n to step $n+1$, each square is divided into 4 identical sub-squares and for each of these sub-squares, one defines a similitude S_i that transforms the vector $\mathbf{V}^{(n)}$ at step n into the vector $\mathbf{V}_i^{(n+1)}$ for the sub-square i at step $n+1$. The so-defined four similitudes must satisfy the vectorial additivity condition:

$$\mathbf{V}^{(n)} = \sum_{i=1}^{4} \mathbf{V}_i^{(n+1)}. \tag{3.2}$$

A straightforward calculation yields the following analytical expression for the partition function scaling exponents $\tau(q)$ (Eq. (2.16)):

$$\tau(q) = -\log_2(p_1^q + p_2^q + p_3^q + p_4^q) - q, \tag{3.3}$$

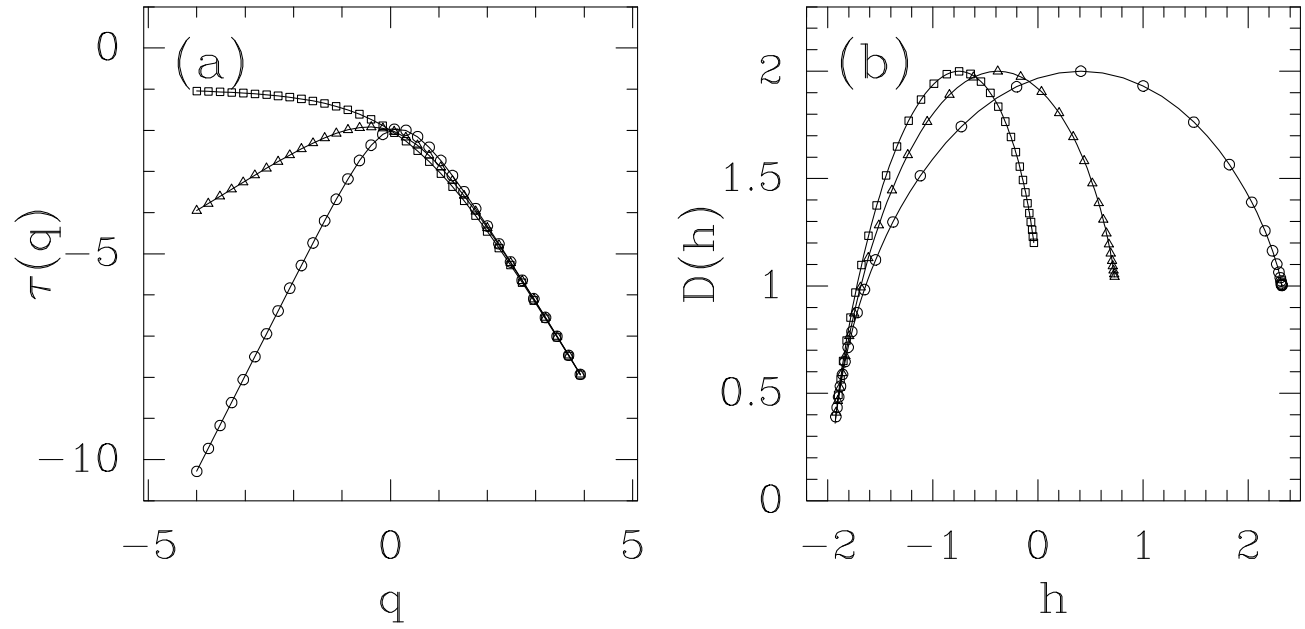

FIG. 2: Theoretical multifractal spectra of the singular vector-valued measures described in Figure 1. (a) $\tau(q)$ spectrum (Eq. (3.3)). (b) $D(h)$ singularity spectrum obtained by Legendre transforming the $\tau(q)$ spectrum (eq. (2.17)). The symbols correspond to the following model parameters: $p_2 = 2$, $p_3 = 1$ and $C = p_1 = p_4 = 0.5$ ((□)), 0.3 ((△)) and 0.1 ((○)).

where p_i, $i = 1$ to 4, are the norms of the similitudes S_i, respectively. Note that this formula is identical to the theoretical spectrum of a nonconservative scalar multinomial measure distributed multiplicatively on the unit square with weights p_i that do not satisfy the conservativity condition $\sum_{i=1}^{4} p_i = 1$ [68, 69]. It is clear, from the example of figure 1, that if the construction process is conservative from a vectorial point of view, it does not conserve the norm of the measure since $\sum_{i=1}^{4} p_i = 4$. In particular, it is remarkable that the vector measures in the left top and right bottom subsquares at construction step 2 are along the y-axis whereas the original vector measure has no component along this axis. By denoting $C = p_1 = p_4 (= 1/2$ in figure 1) this coupling parameter between x and y directions in the construction process, we show in figure 2a that the theoretical $\tau(q)$ spectrum (Eq. (3.3)) is a nonlinear function of q that strongly depends on the value of $0 \leq C \leq 1$. From Legendre transforming Eq. (3.3), one gets a $D(h)$ singularity spectrum with a characteristic multifractal single-humped shape (Fig. 2b) that expands over the interval $[h_{\min}, h_{\max}] = [-1 - \log_2(\max_i p_i), -1 - \log_2(\min_i p_i)]$ and whose maximum $D_F = -\tau(0) = 2$ is the signature that the considered vector-valued measure generated by iterating the rule described in figure 1 is almost everywhere singular on the unit square.

In Fig. 3 are illustrated the main steps of our TWTMM methodology when applied to a $(1024)^2$ realization of a random generalization of the multiplicative construction process described in figure 1. At each successive construction step, the similitudes S_i are randomly permutated. Focusing on the central $(128)^2$ sub-square, we show the singular vector-valued measure (Fig. 3a), the WTMM chains computed with a first order analyzing wavelet at scales $a = 2^2\sigma_W$ (Fig. 3b) and $a = 2^3\sigma_W$ (Fig. 3c), where $\sigma_W = 7$ (pixels) is the smallest resolved scale. On these maxima chains, the black squares correspond to the location of the WTMMM at these scales. The size and the direction of the arrows that originate from these black dots are respectively proportional to the spectral radius $\rho(\mathbf{b}, a)$ and along the eigenvector $\mathbf{G}_\rho(\mathbf{b}, a)$; they allow to visualize $\mathbf{T}_{\boldsymbol{\psi},\rho}[\mathbf{V}](\mathbf{b}, a)$ at the WTMMM. When linking these WTMMM across scales, one gets the set of maxima lines shown in figure 3d as defining the WT skeleton. In figure 4 are reported the results of the computation of the multifractal spectra when averaging the partition functions over 16 $(1024)^2$ realizations of the random vector measure construction process under consideration. As shown in figure 4a, $\mathcal{Z}(q, a)$ (Eq. (2.15)) displays nice scaling behavior over four octaves, when plotted versus a in a logarithmic representation, for $q \in]-2, 4[$ for which statistical convergence turns out to be achieved. A linear regression fit of the data yields the nonlinear $\tau(q)$ spectrum shown in figure 4c, in remarkable agreement with the theoretical spectrum (Eq. (3.3)). This multifractal diagnosis is confirmed in figure 4b where the slope of $h(q, a)$ (Eq. (2.19)) versus $\log_2 a$, clearly depends on q. From the estimate of $h(q)$ (Eq. (2.21)) and $D(q)$ (Eq. (2.22)), one gets the single-humped $D(h)$ curve shown in figure 4d which matches perfectly the theoretical $D(h)$ spectrum obtained by Legendre transforming Eq. (3.3). In figure 4, we have also reported, for comparison, the results obtained when using a box-counting (BC) algorithm adapted to the multifractal analysis of singular vector-valued measures [69, 76, 77, 79]. There is no doubt that BC provides much

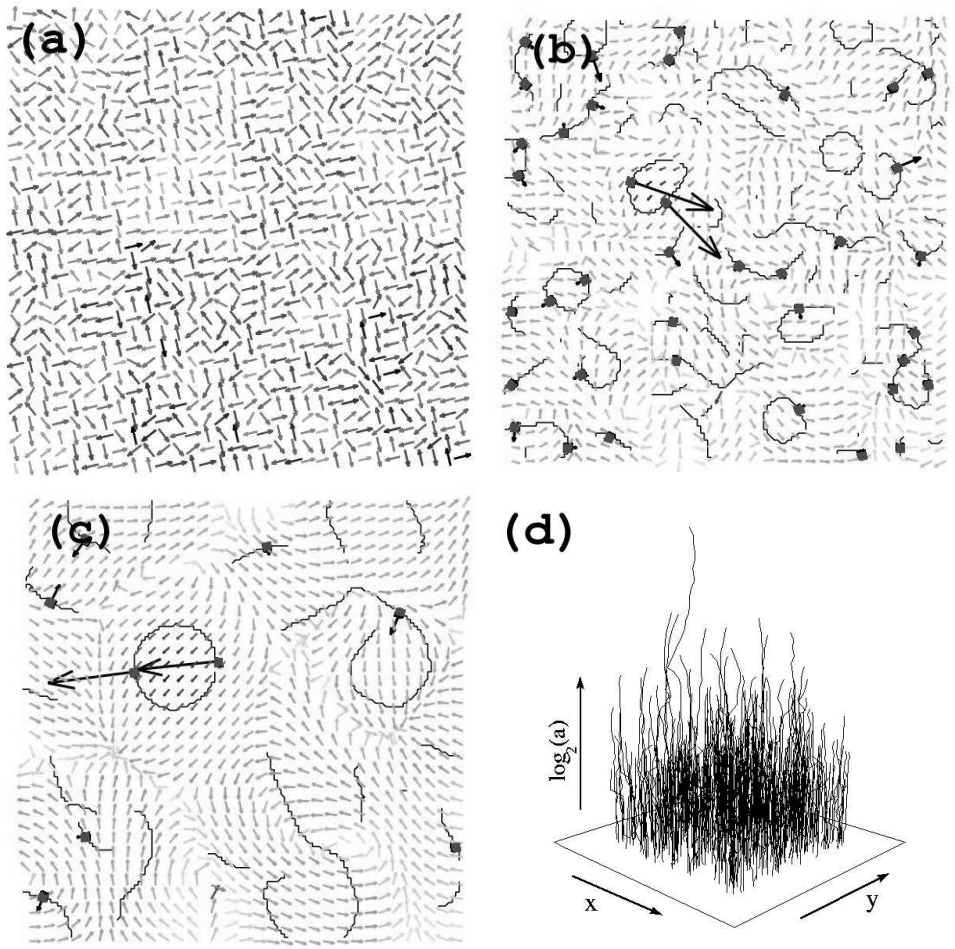

FIG. 3: TWTMM analysis of the 2D vector-valued self-similar measure shown in figure 1 but with systematic random permutation of the S_i at each construction step. The model parameters are $C = 0.5$, $p_2 = 2$ and $p_3 = 1$. ψ is a first-order analyzing wavelet; $\phi(\mathbf{r})$ is the Gaussian function defined in Eq. (2.2). (a) 32 grey-scale coding of the central $(128)^2$ portion of the original $(1024)^2$ field. In (b) $a = 2^2\sigma_W$ and (c) $a = 2^3\sigma_W$, are shown the maxima chains; from the local maxima (WTMMM) of $\mathcal{M}_\psi$ along these chains (■) originates a black arrow whose length is proportional to $\mathcal{M}_\psi$ and direction is along $\mathbf{T}_{\psi,\rho}[\mathbf{V}]$ (Eq. (2.9)). (d) WT skeleton obtained by linking the WTMMM across scales. $\sigma_W = 7$ (pixels) is the characteristic size of ψ at the smallest resolved scale.

poorer results, in particular as far as the estimates of the scaling exponents $\tau(q)$, $h(q)$ and $D(q)$, for negative q values, are concerned. This deficiency mainly results from the fact that the vectorial resultant may be very small (even zero) whereas the norms of the vector measures in the sub-boxes are not small at all. Altogether the results reported in figure 4 bring the demonstration that our TWTMM methodology paves the way from multifractal analysis of singular scalar measures to singular vector measures.

B. Monofractal vector-valued functions

Fractional Brownian motions (fbm) are homogeneous random self-affine functions that have been specifically used to calibrate the 1D [26, 27, 42], 2D [62, 67] and 3D [68, 69] WTMM methodologies. A way to generalize fBm to vector-valued random fields consists in generating independently the d components of such vector fields by fractionally integrating a Gaussian white noise from $\mathbb{R}^d$ into $\mathbb{R}^d$. The multifractal statistical properties of the so-generated fractional Brownian vector fields $\mathbf{B}_H(\mathbf{x})$ ($h_i = H$, $i = 1, 2, .., d$) are characterized by a singularity spectrum which reduces to a single point [69]:

$$\begin{aligned} D(h) &= d \qquad \text{if } h = H\ , \\ &= -\infty \quad \text{if } h \neq H\ . \end{aligned} \tag{3.4}$$

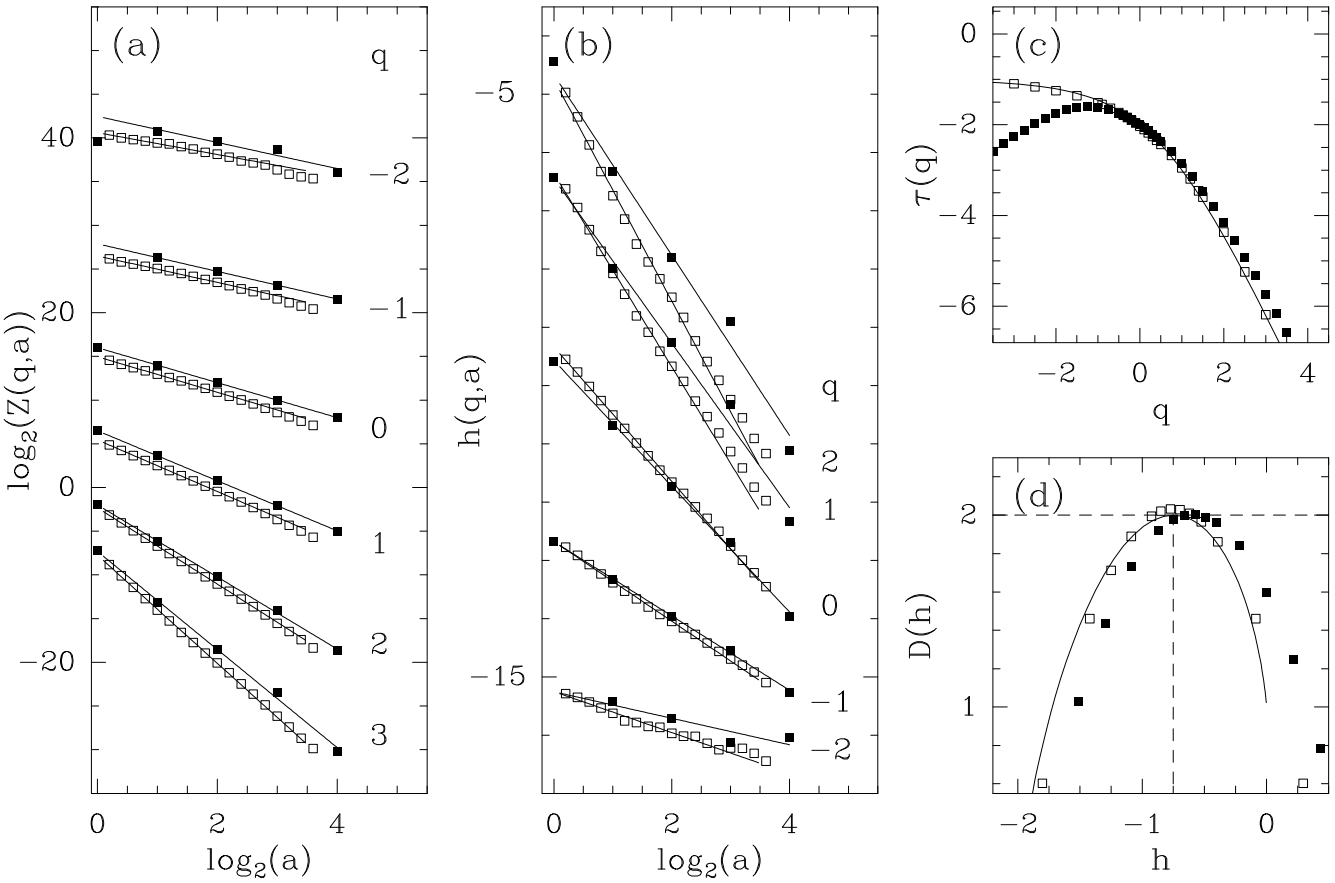

FIG. 4: Multifractal analysis of the 2D vector-valued random measure field (Fig. 3a) using the 2D TWTMM method (□) and box-counting techniques (■). (a) $\log_2 \mathcal{Z}(q,a)$ vs $\log_2 a$; (b) $h(q,a)$ vs $\log_2 a$; the solid lines correspond to linear regression fits over $\sigma_W \lesssim a \lesssim 2^4 \sigma_W$. (c) $\tau(q)$ vs q; the solid line corresponds to the theoretical prediction (Eq. (3.3)). (d) $D(h)$ vs h; the solid line is the Legendre transform of Eq. (3.3). The results reported in this figure correspond to annealed averaging over 16 $(1024)^2$ realizations of the vector-valued random measure construction process. Same analyzing wavelet as in figure 3.

Almost all realizations of $\mathbf{B}_H(\mathbf{x})$ are continuous, everywhere non-differentiable, isotropically scale-invariant as characterized by a unique Hölder exponent $h(\mathbf{x}) = H$, $\forall \mathbf{x}$. By inverse Legendre transforming $D(h)$ according to Eq. (2.17), one gets the following expression for the partition function exponents (Eq. (2.16)):

$$\tau(q) = qH - d\,. \tag{3.5}$$

In figure 5 are illustrated three (128×128) realizations of $\mathbf{B}_H(\mathbf{x})$ for $d = 2$. From a visual inspection of figures 5a ($H = 0.2$), 5b ($H = 0.5$) and 5c ($H = 0.8$), one can convince oneself that this vector-valued random field becomes less and less irregular when increasing the index H. In figure 6 are reported the results of the computation of the $\tau(q)$ and $D(h)$ spectra using the TWTMM method described in Section II. As shown in figure 6a, the annealed average partition functions $\mathcal{Z}(q,a)$ (Eq. (2.15)) over 16 $(1024)^2$ realizations of $\mathbf{B}_{1/2}(\mathbf{x})$, display remarkable scaling behavior over 4 octaves when plotted versus the scale a in a logarithmic representation (Eq. (2.16)). Moreover, for a wide range of values of $q \in [-3, 4]$, the data are in good agreement with the theoretical $\tau(q)$ spectrum (Eq. (3.5)). When proceeding to a linear regression fit of the data over the first four octaves, one gets the linear $\tau(q)$ spectrum shown in figure 6(c) with a slope which slightly underestimates the corresponding $H = 1/2$ exponent. Let us point out that a few percent underestimate has been also reported when preforming similar analysis of 1D [26, 27, 80], 2D [62, 67] and 3D [68] scalar fBm fields. As seen in figure 6b, when plotting $h(q,a)$ vs $\log_2 a$ (Eq. (2.19)), the theoretical Hurst exponent $H = 1/2$ provides an excellent fit of the limiting slope of the data at the smallest available scales ($\sigma_W \lesssim a \lesssim 4\sigma_W$) and this independently of the value of $q \in]-2, 4[$. In figure 6d are reported the corresponding estimates of $D(h)$ from a linear regression fit of $D(q,a)$ vs $\log_2 a$ (Eq. (2.20)) again at small scales. Independently of the value of q, one gets quantitatively comparable values $D(h = H = 1/2) = 2.00 \pm 0.02$. Let us emphasize that as shown in figures 6c and 6d, similar quantitative estimates of both the $\tau(q)$ and $D(h)$ spectra have been obtained for $\mathbf{B}_H(\mathbf{x})$ with $H = 0.2$ and $H = 0.8$. The TWTMM method can thus be considered as having successfully passed the test of homogeneous monofractal stochastic vector-valued fields.

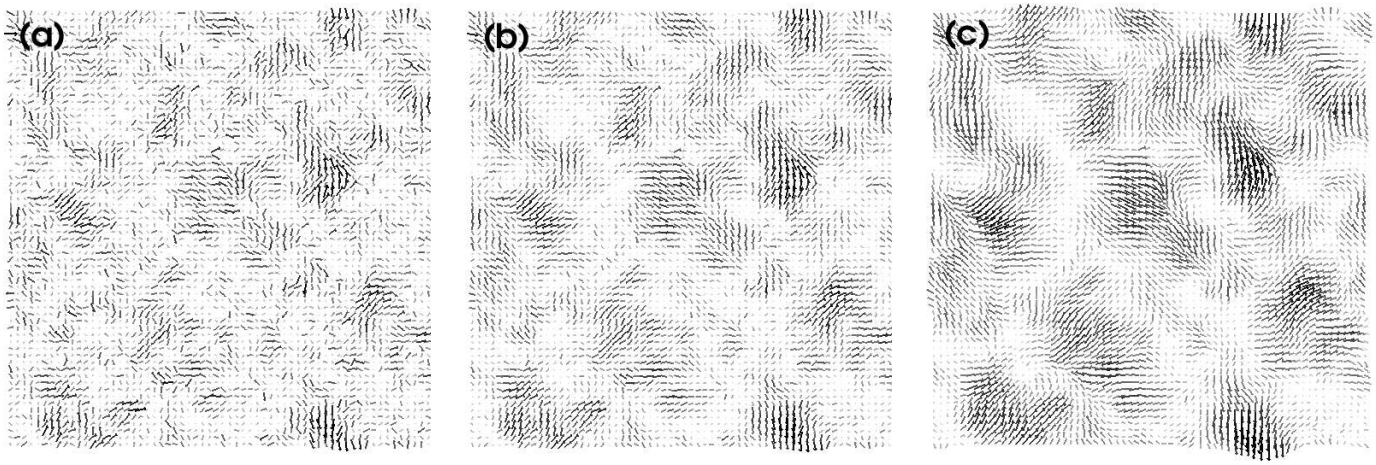

FIG. 5: Fractional Brownian vector-valued fields $\mathbf{B}_H(\mathbf{x})$ (128×128) generated by Fourier transform filtering of two independent realizations of a Gaussian white noise from $\mathbb{R}^2$ into $\mathbb{R}$. (a) $H = 0.2$; (b) $H = 0.5$; (c) $H = 0.8$. The norm of $\mathbf{B}_H(\mathbf{x})$ is represented using a gray scale coding frow white (min) to black (max).

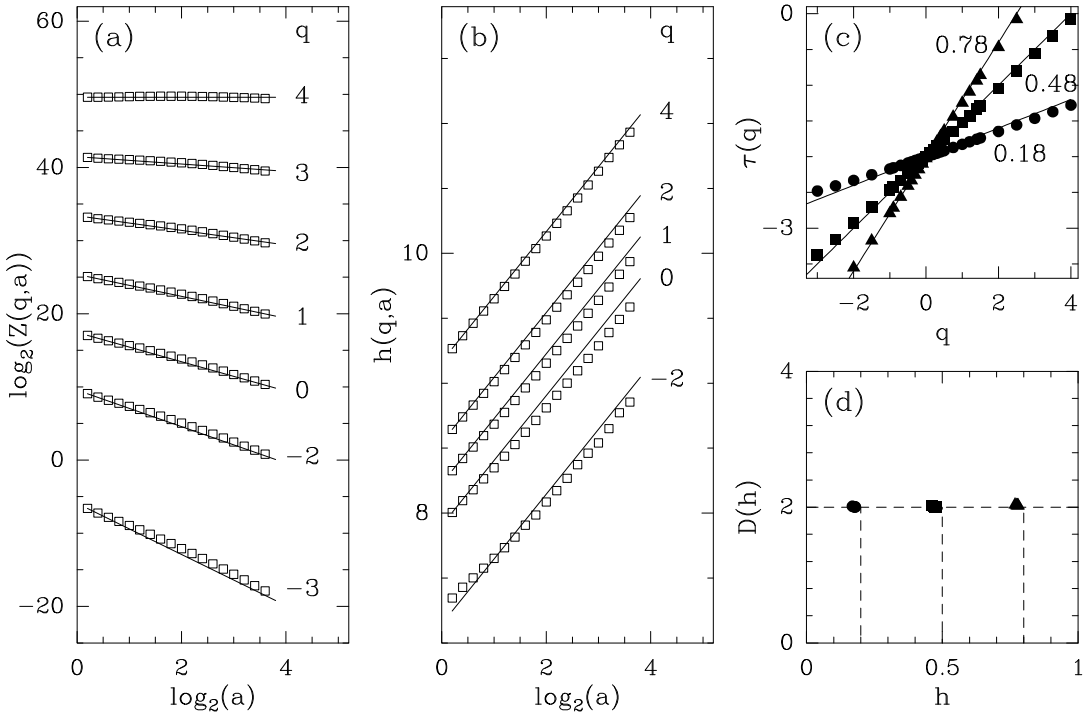

FIG. 6: Determination of the $\tau(q)$ and $D(h)$ spectra of (1024×1024) fractional Brownian vector-valued fields $\mathbf{B}_H(\mathbf{x})$ with the TWTMM method. (a) $\log_2 \mathcal{Z}(q,a)$ vs $\log_2 a$, for $\mathbf{B}_{H=1/2}(\mathbf{r})$; the solid lines correspond to the theoretical predictions $\tau(q) = q/2 - 2$ (Eq. (3.5)) for the corresponding values of q. (b) $h(q,a)$ vs $\log_2 a$; the solid lines correspond to the theoretical slope $H = 1/2$. (c) $\tau(q)$ vs q for $H = 0.2$ (•), 0.5 (■) and 0.8 (▲); the solid lines correspond to linear regression fit estimates of H. (d) $D(h)$ vs h obtained from the estimates of $h(q)$ (Eq. (2.21)) and $D(q)$ (Eq. (2.22)) via the scaling bahavior of $h(q,a)$ (Eq. (2.19)) and $D(q,a)$ (Eq. (2.20)) respectively; the symbols have the same meaning as in (c). The analyzing wavelet is the third-order wavelet generated using the isotropic mexican hat smoothing function $\phi(\mathbf{x})$ (Eq. (2.3)). These results correspond to annealed averaging over 16 (1024×1024) realizations of $\mathbf{B}_H(\mathbf{x})$. a is expressed in σ_W ($= 13$ pixels) units.

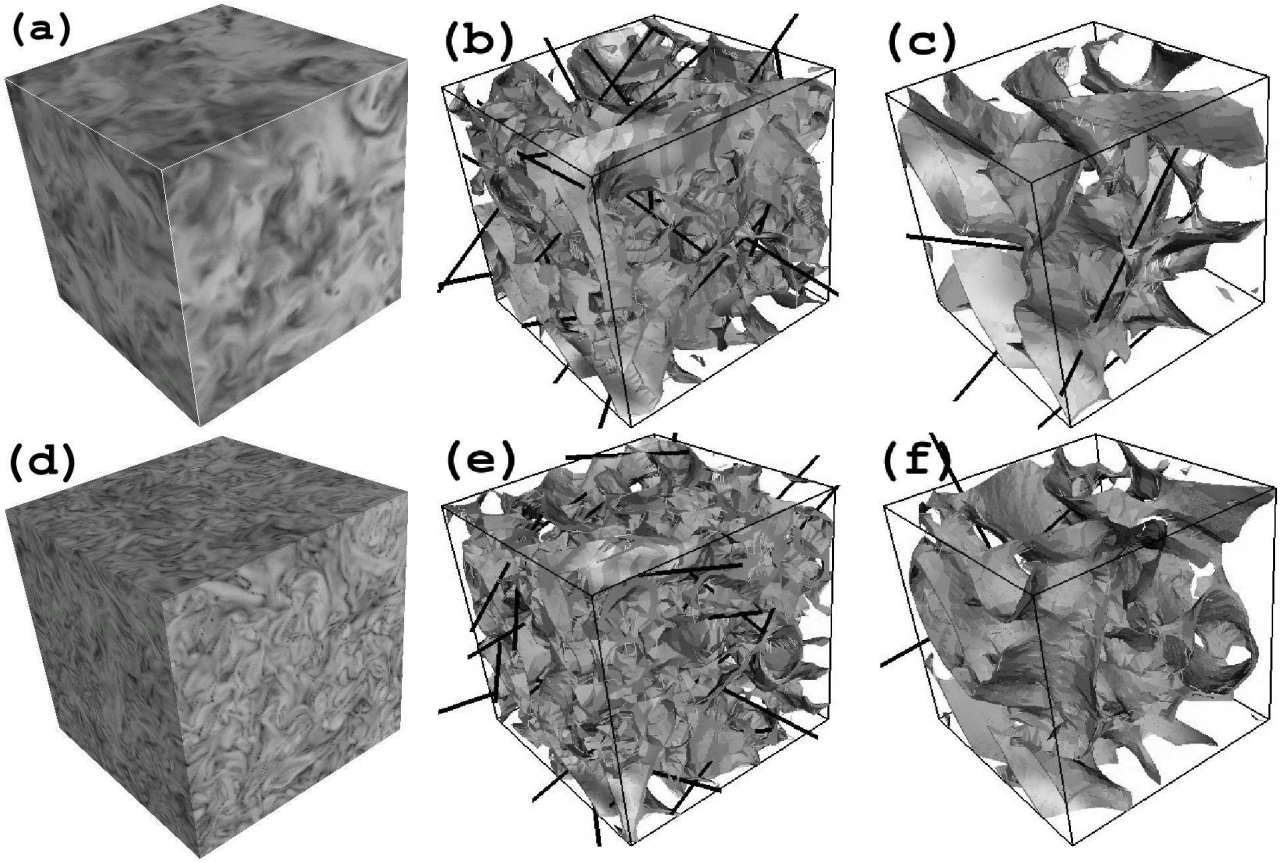

FIG. 7: 3D wavelet transform analysis of the velocity and vorticity fields from $(256)^3$ DNS by Lévêque ($R_\lambda = 140$). ψ is the third-order radially symmetric analyzing wavelet (the smoothing function $\phi(\mathbf{x})$ is the isotropic mexican hat defined in Eq. (2.3)). **Velocity field:** (a) A snapshot of $\boldsymbol{v}(\mathbf{x})$ using a 64 gray level coding of $|\boldsymbol{v}|$ on the three visible sides of the $(256)^3$ cube; in (b) $a = 2^2\sigma_W$ and (c) $a = 2^3\sigma_W$, are shown the WT modulus maxima surfaces; from the local maxima (WTMMM) of $\mathcal{M}_\psi$ (Eq. (2.10)) along these surfaces originates a black segment whose length is proportional to $\mathcal{M}_\psi$ and direction is along $\mathbf{G}_\rho(\mathbf{x}, a)$ (Eq. (2.9)). **Vorticity field:** (d), (e) and (f) are equivalent to (a), (b) and (c) but for the vorticity field $\boldsymbol{\omega}(\mathbf{x})$. $\sigma_W = 13$ pixels.

IV. APPLICATION OF THE TWTMM METHOD TO VELOCITY AND VORTICITY FIELDS FROM DIRECT NUMERICAL SIMULATIONS OF THE INCOMPRESSIBLE NAVIER-STOKES EQUATIONS

This section is devoted to the application of the TWTMM method to the velocity ($\boldsymbol{v}$) and vorticity ($\boldsymbol{\omega}$) fields from DNS of isotropic turbulence carried out by Lévêque using a pseudo spectral method solver. The DNS were performed using 256^3 mesh points in a 3D periodic box. The Taylor microscale is $R_\lambda = 140$. Here we will examine only one snapshot of the velocity (Fig. 7a) and vorticity (Fig. 7d) spatial fields. We will mainly proceed to a comparative multifractal analysis based on the estimate of the corresponding $\tau(q)$ and $D(h)$ spectra from some annealed averaging of the partition functions over 18 different snapshots.

A. Velocity field

In figure 7(a-c) are illustrated the main steps of our TWTMM analysis of the velocity field $\boldsymbol{v}(\mathbf{x})$. Figure 7a shows a 3D representation of the spatial profile of $|\boldsymbol{v}|$ using a 64 gray level coding. In figures 7b and 7c are shown the WTMM maxima surfaces along with the WTMMM points as computed with a third-order analyzing wavelet at the scales $a = 2^2\sigma_W$ and $a = 2^3\sigma_W$ respectively ($\sigma_W = 13$ pixels is the smallest resolved scale). From these WTMMM originate a black segment whose length is proportional to $\mathcal{M}_\psi$ (Eq. (2.10)) and direction is along $\mathbf{G}_\rho(\mathbf{x}, a)$ (Eq. (2.9)). The results of the computation of the $\tau(q)$ and $D(h)$ spectra are reported in figure 8. As shown in figures 8a and 8b, both the $\mathcal{Z}(q, a)$ (Eqs. (2.15) and (2.16)) and $h(q, a)$ (Eq. (2.19)) partition functions display rather nice scaling properties for $q = -4$ to 6, except at small scales ($a \lesssim 2^{1.5}\sigma_W$) where some curvature is observed in the log-log plots as induced

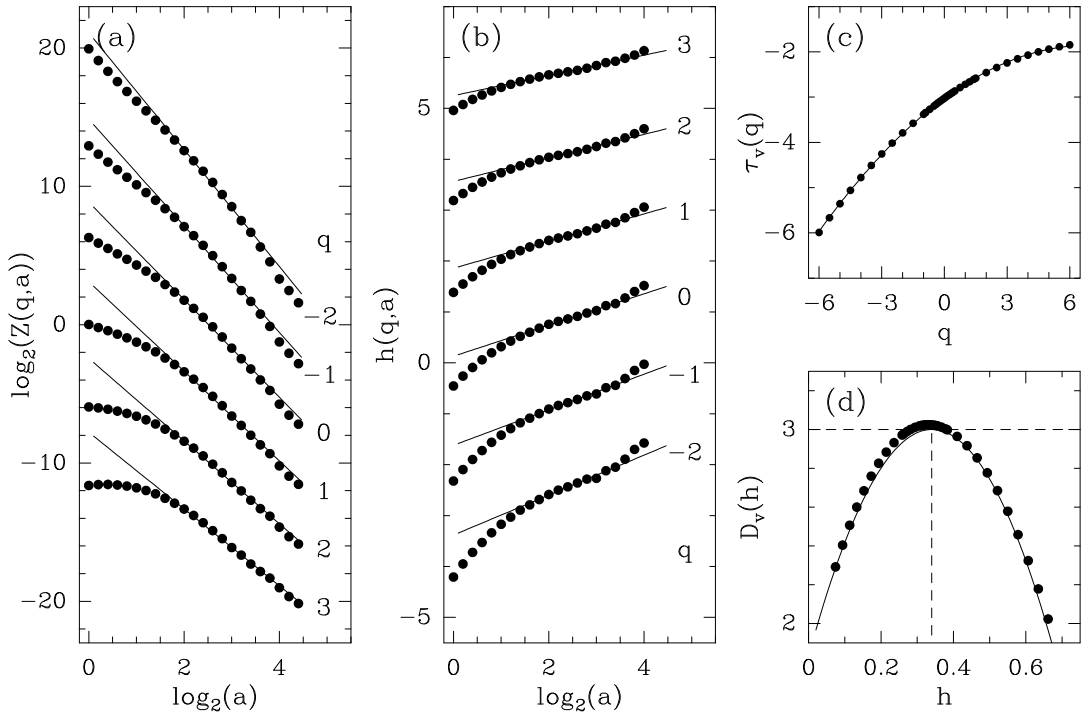

FIG. 8: Determination of the $\tau_{\boldsymbol{v}}(q)$ and $D_{\boldsymbol{v}}(h)$ spectra of the velocity field with the TWTMM method. The analyzing wavelet is the same as in figure 7. (a) $\log_2 \mathcal{Z}(q,a)$ vs $\log_2 a$; (b) $h(q,a)$ vs $\log_2 a$; the solid lines correspond to linear regression fit estimates in the range $2^{1.2}\sigma_W \lesssim a \lesssim 2^{3.5}\sigma_W$. (c) $\tau_{\boldsymbol{v}}(q)$ vs q; the solid line corresponds to a fit of the data with the log-normal parabolic spectrum (4.1) for the parameter values $C_0^{\boldsymbol{v}} = 3.02$, $C_1^{\boldsymbol{v}} = -0.34$ and $C_2^{\boldsymbol{v}} = 0.049$ (Eq. (4.2)). (d) $D_{\boldsymbol{v}}(h)$ vs h, as obtained from the scaling behavior of $h(q,a)$ (Eq. (2.19)) and $D(q,a)$ (Eq. (2.20)); the solid line corresponds to a fit of the data with the log-normal parabolic spectrum (4.3) with the same parameter values (Eq. (4.2)). These results correspond to annealed averaging over 18 $(256)^3$ snapshots of $\boldsymbol{v}(\mathbf{x})$. a is expressed in σ_W ($= 13$ pixels) units.

by dissipation effects [81–83]. Linear regression fit of the data in figure 8a in the range $2^{1.5}\sigma_W \lesssim a \lesssim 2^{4.1}\sigma_W$, yields the increasing non-linear $\tau_{\boldsymbol{v}}(q)$ curve shown in figure 8c, the hallmark of multifractal continuous vector-valued fields. Actually, this spectrum is quite well fitted by a parabola as predicted for log-normal statistics [45, 48, 84–86]:

$$\tau_{\boldsymbol{v}}(q) = -C_0^{\boldsymbol{v}} - C_1^{\boldsymbol{v}} q - C_2^{\boldsymbol{v}} \frac{q^2}{2}, \tag{4.1}$$

with the following parameter values

$$C_0^{\boldsymbol{v}} = 3.02 \pm 0.02, \quad C_1^{\boldsymbol{v}} = -0.34 \pm 0.02, \quad C_2^{\boldsymbol{v}} = 0.049 \pm 0.003. \tag{4.2}$$

The corresponding singularity spectrum $D_{\boldsymbol{v}}(h)$ obtained from the scaling behavior of the partition functions $h(q,a)$ (Eqs. (2.19) and (2.21)) and $D(q,a)$ (Eqs. (2.20) and (2.22)) is shown in figure 8d. Consistently, the data points fall on a parabola which is well fitted by the Legendre transform of Eq. (4.1), namely:

$$D_{\boldsymbol{v}}(h) = C_0^{\boldsymbol{v}} - \frac{(h + C_1^{\boldsymbol{v}})^2}{2C_2^{\boldsymbol{v}}}, \tag{4.3}$$

for the same parameter values as previously obtained in Eq. (4.2). The velocity field is thus found singular almost everywhere: $C_0^{\boldsymbol{v}} = -\tau_{\boldsymbol{v}}(q=0) = D_{\boldsymbol{v}}(q=0) = 3.02 \pm 0.02$. The most frequent Hölder exponent $h(q=0) = -C_1$ (corresponding to the maximum of $D(h)$) takes the value $-C_1^{\boldsymbol{v}} = 0.34 \pm 0.02$ which is much closer to the Kolmogorov (1941) prediction $h = 1/3$ [22, 23, 87], than previous experimental measurements ($h \simeq 0.39 \pm 0.02$) based on the analysis of the longitudinal velocity fluctuations [48]. As far the intermittency coefficient $C_2^{\boldsymbol{v}}$ (that characterizes the width of $D_{\boldsymbol{v}}(h)$) is concerned, one gets a value $C_2^{\boldsymbol{v}} = 0.049 \pm 0.003$ which is much larger than the estimate $C_2 = 0.025 \pm 0.003$ obtained for the 1D longitudinal velocity increment statistics [45, 48, 85, 86]. Actually this estimate is comparable but still slightly larger than the value $C_2 \simeq 0.04$ extracted from the experimental analysis of transverse velocity increments [85, 88–94]. Even though one has to be cautious as regard to the rather modest value

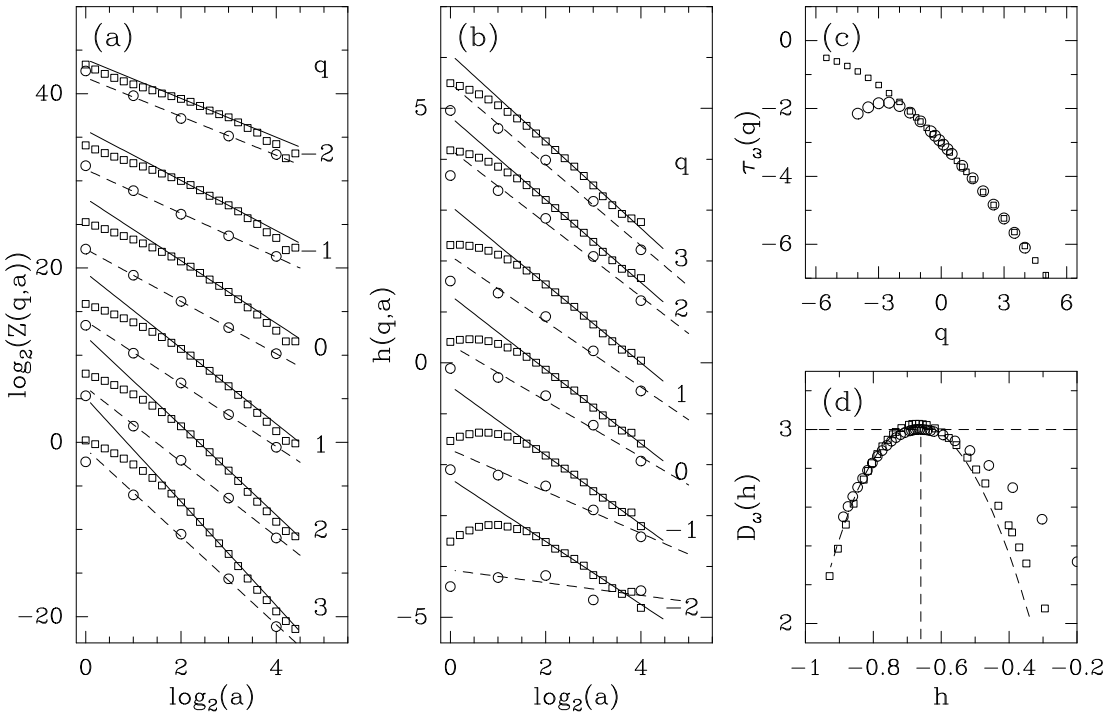

FIG. 9: Determination of the $\tau_{\boldsymbol{\omega}}(q)$ and $D_{\boldsymbol{\omega}}(h)$ spectra of the vorticity field with the TWTMM method (□), with the same analyzing wavelet as in figure 7, and with box-counting techniques (○). (a) $\log_2 \mathcal{Z}(q,a)$ vs $\log_2 a$; (b) $h(q,a)$ vs $\log_2 a$; the solid and dashed lines correspond to linear regression fit estimates in the range $2^{1.2}\sigma_W \lesssim a \lesssim 2^{3.5}\sigma_W$. (c) $\tau_{\boldsymbol{\omega}}(q)$ vs q; (d) $D_{\boldsymbol{\omega}}(h)$ vs h as obtained from the scaling behavior of $h(q,a)$ (Eq. (2.19)) and $D(q,a)$ (Eq. (2.20)); the dashed line corresponds to the parabolic spectrum found for $\boldsymbol{v}$ in figure 8d (Eqs. (4.2) and (4.3)); after a translation of one unit on the left (Eqs. (4.4) and (4.5)); the dashed vertical line marks the K41 value $h_{\boldsymbol{\omega}} = h_{\boldsymbol{v}} - 1 = -2/3$. These results correspond to annealed averaging over 18 $(256)^3$ snapshots of $\boldsymbol{\omega}(\mathbf{x})$. a is expressed in σ_W (= 13 pixels) units.

of $R_\lambda = 140$ of the analyzed DNS data, it is not so surprising that when investigating the full 3D fluctuations of the velocity field, one realizes that this field is much more intermittent than previously estimated from the fluctuations of one of its component only.

B. Vorticity field

In figures 7d-f are shown for comparison the main steps of our TWTMM analysis of the vorticity field $\boldsymbol{\omega} = \boldsymbol{\nabla} \wedge \boldsymbol{v}$. The results of the computation of the multifractal spectra $\tau_{\boldsymbol{\omega}}(q)$ and $D_{\boldsymbol{\omega}}(h)$ with the TWTMM method are shown in figure 9 (symbols (□)). The partition function $\mathcal{Z}(q,a)$ (Fig. 9a) and $h(q,a)$ (Fig. 9b) display rather convincing scaling behavior in the range $2^{1.8}\sigma_W \lesssim a \lesssim 2^{3.2}\sigma_W$ for values of $q \in [-4,6]$. At smaller scales $a \lesssim 2^{1.8}\sigma_W$, one again observes a clear bending of the data curves as the signature of viscous effects [81–83]. As shown in figure 9c, the $\tau_{\boldsymbol{\omega}}(q)$ spectrum estimated by linear regression fit of the $\mathcal{Z}(q,a)$ data in figure 9a, is a definite decreasing non-linear function similar to the one obtained for the singular vector-value measures in figure 4c; hence $h(q) = \partial\tau(q)/\partial q < 0$ and the support of the $D_{\boldsymbol{\omega}}(h)$ singularity spectrum expands over negative h values as confirmed in figure 9d where the data points have been extracted from the scaling behavior of $h(q,a)$ (Eqs. (2.19) and (2.21)) and $D(q,a)$ (Eqs. (2.20) and (2.22)).

What is quite remarkable with the results reported in figures 8 and 9, is the fact that, up to statistical uncertainty, the data for $h(q,a)$ in figures 8b and 9b strongly suggest the validity of the following relationship [69, 77]:

$$h_{\boldsymbol{\omega}}(q) = h_{\boldsymbol{v}}(q) - 1. \tag{4.4}$$

Actually, as shown in figure 9d, both singularity spectra $D_{\boldsymbol{\omega}}(h)$ (symbols (□)) and $D_{\boldsymbol{v}}(h)$ (dashed line) are likely to coincide after translating the later by one unit on the left. Some slight difference can be noticed for the right decreasing branch of these spectra which actually is a consequence of the largest error bars obtained for the negative values of $q \leq -2$. Even though one could have guessed the results reported in figures 8 and 9 by noticing that $\boldsymbol{\omega} = \boldsymbol{\nabla} \wedge \boldsymbol{v}$

involves first derivatives of $\boldsymbol{v}$ only, they bring, to our knowledge, the first numerical evidence that the singularity spectra of $\boldsymbol{v}$ and $\boldsymbol{\omega}$ are likely to be intimately related and to satisfy the equation:

$$D_{\boldsymbol{\omega}}(h) = D_{\boldsymbol{v}}(h+1). \tag{4.5}$$

More precisely the $\tau_{\boldsymbol{\omega}}(q)$ and $D_{\boldsymbol{\omega}}(h)$ spectra can again be very well fitted by a parabola of Eqs. (4.1) and (4.3) respectively, with the following parameter values:

$$C_0^{\boldsymbol{\omega}} = 3.01 \pm 0.02, \quad C_1^{\boldsymbol{\omega}} = 0.66 \pm 0.02, \quad C_2^{\boldsymbol{\omega}} = 0.055 \pm 0.004. \tag{4.6}$$

When comparing the parameter values to those found for the velocity in Eq. (4.2), one gets quite consistent estimates. In particular the most frequent Hölder exponent corresponding to the maximum of the singularity spectrum satisfies Eq. (4.4): $-C_1^{\boldsymbol{\omega}} = -0.66 \pm 0.02 \simeq -C_1^{\boldsymbol{v}} - 1$, and therefore confirms the statistical predominance of singularities of strength $h^{\boldsymbol{\omega}} = -2/3$, accordingly to K41 theoretical prediction $h^{\boldsymbol{v}} = 1/3$ [22, 23, 87].

In figure 9, we have also reported for comparison the estimates of the $\tau^{\boldsymbol{\omega}}(q)$ and $D^{\boldsymbol{\omega}}(h)$ spectra when using classical box-counting techniques [69]. The results obtained for positive q values ($0 \leq q \leq 6$) are in good agreement with those obtained with our TWTMM methodology. This is no longer true for negative q values for which, very much like what have already been observed for multifractal vector valued measures in figure 4, the box-counting techniques fail to master the scaling behavior of the partition functions $\mathcal{Z}(q,a)$, $h(q,a)$ and $D(q,a)$. This justifies, a posteriori, the need of elaborating and implementing a new wavelet based methodology for multifractal analysis of multidimensional vector-valued random fields.

V. CONCLUSION AND PERSPECTIVES

To summarize, we have extended the wavelet based multifractal formalism to vector-valued random fields [69, 77]. Indeed we believe that the generalization of the 1D [26–28, 36], 2D [62, 63, 67] and 3D [68, 69] WTMM methodology to vector-valued multidimensional fields is likely to provide a unified theoretical framework for the application of fractal and multifractal concepts to various situations in fundamental as well as applied sciences. In particular, we hope that the new algorithms we have implemented and the new softwares we have developed, will become as useful to characterizing the roughness fluctuations of scalar and vector-valued fields as the well known phase portrait reconstruction, Poincaré section and first return map techniques for the analysis of chaotic times series [95–98]. Moreover, besides the technical aspect and the potential interest for future applications, there is also some very promising perspectives on the theoretical side. Actually, if our phenomenological approach has provided some keys towards a unified multifractal statistical formalism for scalar and vector-valued fields, there is clearly a need to extend in higher dimensions the rigorous mathematical results derived for the 1D WTMM method in Refs. [36, 37].

As far as the results of the application of the TWTMM method to DNS turbulence data reported in Section IV, they have clearly revealed the existence of an intimate relationship between the velocity and the vorticity 3D statistics that turn out to be significantly more intermittent than previously estimated from the statistics of 1D longitudinal velocity increments. The multifractal spectra of both the velocity and the vorticity fields were shown to be very well fitted by parabolic curves consistantly with the log-normal picture proposed by Kolmogorov [99] and Obukhov [100] in 1962, to account for the intermittency corrections to K41 theory [87]. In the context of fully developed turbulence numerical data analysis, the TWTMM method looks very promising to many extents. By applying the 3D WTMM method to the dissipation and enstrophy scalar fields [68, 69] and the 3D TWTMM method to the velocity and vorticity fields [69, 77], one can plan to revisit previous comparative studies of the statistics of these scalar and vector-valued fields. In particular, several experiments and numerical works [13, 70, 73, 101–114] have tested various facets of the so-called refined similarity hypothesis (RSH) [99, 100] between the statistics of the dissipation and the longitudinal velocity increments. Nevertheless, so far, the support for the RSH is strong but not unequivocal. Pioneering [115, 116] as well as more recent [68, 69, 117] numerical DNS studies have shown that the enstrophy field is more intermittent than the dissipation field. As suggested by Chen *et al.* [94], this difference is likely to result from the difference observed in the scaling exponents ζ_p^L and ζ_p^T of longitudinal and transverse velocity structure functions, respectively [85, 88–93]. More precisely, Chen *et al.* [94] reported numerical results that demonstrate the possible validity of a different RSH for the transverse direction (RSHT) that connects the statistics of the transverse velocity increments to the locally averaged enstrophy in the inertial range. The important implication of RSHT is the possible existence of two independent sets of scaling exponents respectively related to the symmetric (dissipation physics) and antisymmetric (vortex dynamics) parts of the strain rate. But these results deserve further confirmation and some caution should be taken when extrapolating them to high Reynolds numbers since different theoretical studies have converged to the conclusion that asymptotic scaling exponents must be equal in the limit $R_\lambda \to \infty$ [118–122]. Finally,

the actual role of coherent and/or localized structures like vorticity filaments in the intermittent nature of turbulent flows is still debated. In the past decade, the observation and the characterization of well organized structures have received some renewed interest from both a numerical [115, 123–131] and an experimental [46, 132–142] point of view. Thanks to the singular value decomposition, one has a way to focus on fluctuations that are locally confined in 2D ($\min_i \sigma_i = 0$, $i = 1, 2, 3$ in Eq. (2.7)) or in 1D (the two smallest σ_i are zero) and then simultaneously proceed to a multifractal and structural analysis of turbulent flows. The investigation along this line of vorticity sheets and vorticity filaments in DNS of the incompressible Navier-Stokes equations is in current progress. We hope to elaborate on the results of this study in a forthcoming publication.

Acknowledgments

We are very endebted to E. Lévêque for allowing us to have access to his DNS numerical data and to the CNRS under GDR turbulence.

---

[1] P. Hubert, Y. Tessier, S. Lovejoy, D. Schertzer, F. Schmitt, P. Ladoy, J. P. Carbonnel, S. Violette, and I. Desurosne, Geophys. Res. Lett., **20**(10), 931, (1993).
[2] P. Burlando, and R. Rosso, J. Hydrol., **187**, 45 (1996).
[3] H. Bendjoudi, P. Hubert, D. Schertzer, and S. Lovejoy, Geosci. Surface Hydrol., **325**, 323 (1997).
[4] D. Veneziano, and P. Furcolo, Water Resour. Res., **38**(12), 1306 (2002).
[5] C. De Michele, N. T. Kottegoda, and R. Rosso, Water Sci. Technol., **45**(2), 83 (2002).
[6] J. J. Castro, A. A. Carsteanu, and C. G. Flores, Physica A **33**, 206 (2004).
[7] T. C. Halsey, M. H. Jensen, L. P. Kadanoff, I. Procaccia, and B. I. Schraiman, Phys. Rev. A **33**, 1141 (1986).
[8] P. Collet, J. Lebowitz, and A. Porzio, J. Stat. Phys. **47**, 609 (1987).
[9] D. Rand, Ergod. Th. and Dyn. Sys. **9**, 527 (1989).
[10] B. B. Mandelbrot, J. Fluid Mech. **62**, 331 (1974).
[11] G. Paladin and A. Vulpiani, Phys. Rep. **156**, 148 (1987).
[12] B. B. Mandelbrot, *Fractals and Multifractals : Noise, Turbulence and Galaxies*, Vol. 1 of *Selecta* (Springer Verlag, Berlin, 1989).
[13] C. Meneveau and K. R. Sreenivasan, J. Fluid Mech. **224**, 429 (1991).
[14] P. Grassberger and I. Procaccia, Phys. Rev. Lett. **50**, 346 (1983); Physica D **9**, 189 (1983).
[15] R. Badii and A. Politi, Phys. Rev. Lett. **52**, 1661 (1984); J. Stat. Phys. **40**, 725 (1985).
[16] P. Grassberger, R. Badii, and A. Politi, J. Stat. Phys. **51**, 135 (1988).
[17] F. Argoul, A. Arneodo, J. Elezgaray, G. Grasseau, and R. Murenzi, Phys. Rev. A **41**, 5537 (1990).
[18] L. V. Meisel, M. Jonhson, and P. J. Cote, Phys. Rev. A **45**, 6989 (1992).
[19] B. B. Mandelbrot, *Fractals : Form, Chance and Dimensions* (Freeman, San Francisco, 1977); *The Fractal Geometry of Nature* (Freeman, San Francisco, 1982).
[20] H. O. Peitgen and D. Saupe, Eds., *The Science of Fractal Images* (Springer Verlag, New York, 1987).
[21] G. Parisi and U. Frisch, in *Turbulence and Predictability in Geophysical Fluid Dynamics and Climate Dynamics*, *Proc. of Int. School*, edited by M. Ghil, R. Benzi, and G. Parisi (North-Holland, Amsterdam, 1985), p. 84.
[22] A. S. Monin and A. M. Yaglom, *Statistical Fluid Mechanics* (MIT Press, Cambridge, MA, 1975), Vol. 2.
[23] U. Frisch, *Turbulence* (Cambridge Univ. Press, Cambridge, 1995).
[24] A. L. Barabási and T. Vicsek, Phys. Rev. A **44**, 2730 (1991).
[25] A. L. Barabási, P. Széfalusy, and T. Vicsek, Physica A **178**, 17 (1991).
[26] J. F. Muzy, E. Bacry, and A. Arneodo, Phys. Rev. Lett. **67**, 3515 (1991); Int. J. of Bifurcation and Chaos **4**, 245 (1994).
[27] A. Arneodo, E. Bacry, and J. F. Muzy, Physica A **213**, 232 (1995).
[28] J. F. Muzy, E. Bacry, and A. Arneodo, Phys. Rev. E **47**, 875 (1993).
[29] P. Goupillaud, A. Grossmann, and J. Morlet, Geoexploration **23**, 85 (1984).
[30] A. Grossmann and J. Morlet, S.I.A.M. J. Math. Anal **15**, 723 (1984).
[31] Y. Meyer, *Ondelettes* (Herman, Paris, 1990).
[32] I. Daubechies, *Ten Lectures on Wavelets* (SIAM, Philadelphia, 1992).
[33] S. Mallat, *A Wavelet Tour in Signal Processing* (Academic Press, New York, 1998).
[34] S. Mallat and S. Zhong, IEEE Trans. on Pattern Analysis and Machine Intelligence **14**, 710 (1992).
[35] S. Mallat and W. L. Hwang, IEEE Trans. on Information Theory **38**, 617 (1992).
[36] E. Bacry, J. F. Muzy, and A. Arneodo, J. Stat. Phys. **70**, 635 (1993).
[37] S. Jaffard, SIAM J. Math. Anal. **28**, 944 (1997).
[38] H. G. E. Hentschel, Phys. Rev. E **50**, 243 (1994).
[39] A. Arneodo, E. Bacry, and J. F. Muzy, Phys. Rev. Lett. **74**, 4823 (1995).

[40] A. Arneodo, E. Bacry, S. Jaffard, and J. F. Muzy, J. Stat. Phys. **87**, 179 (1997); J. of Fourier Analysis and Applications **4**, 159 (1998); CRM Proceedings and Lecture Notes **18**, 315 (1999).
[41] J. C. Vassilicos and J. C. Hunt, Proc. Roy. Soc. Lond. **435**, 505 (1991).
[42] A. Arneodo, F. Argoul, E. Bacry, J. Elezgaray, and J. F. Muzy, *Ondelettes, Multifractales et Turbulences : de l'ADN aux croissances cristallines* (Diderot Editeur, Art et Sciences, Paris, 1995).
[43] A. Arneodo, B. Audit, N. Decoster, J. F. Muzy, and C. Vaillant, in *The Science of Disasters : climate disruptions, heart attacks and market crashes*, edited by A. Bunde, J. Kropp, and H. J. Schellnhuber (Springer Verlag, Berlin, 2002), p. 27.
[44] A. Arneodo, J. F. Muzy, and S. G. Roux, J. Phys. II France **7**, 363 (1997).
[45] A. Arneodo, S. Manneville, and J. F. Muzy, Eur. Phys. J. B **1**, 129 (1998).
[46] S. G. Roux, J. F. Muzy, and A. Arneodo, Eur. Phys. J. B **8**, 301 (1999).
[47] A. Arneodo, S. Manneville, J. F. Muzy, and S. G. Roux, Phil. Trans. R. Soc. London A **357**, 2415 (1999).
[48] J. Delour, J. F. Muzy, and A. Arneodo, Eur. Phys. J. B **23**, 243 (2001).
[49] A. Arneodo, E. Bacry, P. V. Graves, and J. F. Muzy, Phys. Rev. Lett. **74**, 3293 (1995).
[50] A. Arneodo, Y. d'Aubenton-Carafa, E. Bacry, P. V. Graves, J. F. Muzy, and C. Thermes, Physica D **96**, 291 (1996).
[51] B. Audit, C. Thermes, C. Vaillant, Y. d'Aubenton-Carafa, J. F. Muzy, and A. Arneodo, Phys. Rev. Lett. **86**, 2471 (2001).
[52] B. Audit, C. Vaillant, A. Arneodo, Y. d'Aubenton-Carafa, and C. Thermes, J. Mol. Biol. **316**, 903 (2002).
[53] A. Arneodo, J. F. Muzy, and D. Sornette, Eur. Phys. J. B **2**, 277 (1998).
[54] J. F. Muzy, D. Sornette, J. Delour, and A. Arneodo, Quantitative Finance **1**, 131 (2000).
[55] P. C. Ivanov, M. G. Rosenblum, C. K. Peng, J. Mietus, S. Havlin, H. E. Stanley, and A. L. Goldberger, Nature **383**, 323 (1996).
[56] P. C. Ivanov, L. A. Nunes Amaral, A. L. Goldberger, S. Havlin, M. G. Rosenblum, Z. R. Struzik, and H. E. Stanley, Nature **399**, 461 (1999).
[57] A. Arneodo, F. Argoul, E. Bacry, J. F. Muzy, and M. Tabard, Phys. Rev. Lett. **68**, 3456 (1992).
[58] A. Arneodo, F. Argoul, J. F. Muzy, M. Tabard, and E. Bacry, Fractals **1**, 629 (1993).
[59] A. Arneodo, F. Argoul, J. F. Muzy, and M. Tabard, Phys. Lett. A **171**, 31 (1992); Physica A **188**, 217 (1992).
[60] A. Khun, F. Argoul, J. F. Muzy, and A. Arneodo, Phys. Rev. Lett. **73**, 2998 (1994).
[61] J. Arrault, A. Arneodo, A. Davis, and A. Marshak, Phys. Rev. Lett. **79**, 75 (1997).
[62] A. Arneodo, N. Decoster, and S. G. Roux, Phys. Rev. Lett. **83**, 1255 (1999); Eur. Phys. J. B **15**, 567 (2000).
[63] N. Decoster, S. G. Roux, and A. Arneodo, Eur. Phys. J. B **15**, 739 (2000).
[64] S. G. Roux, A. Arneodo, and N. Decoster, Eur. Phys. J. B **15**, 765 (2000).
[65] A. Khalil, G. Joncas, F. Nekka, P. Kestener, and A. Arneodo, "Morphological analysis of H1 features. II Wavelet-based multifractal formalism", preprint (2004).
[66] P. Kestener, J. M. Lina, P. Saint-Jean, and A. Arneodo, Image Anal. Stereol. **20**, 169 (2001).
[67] A. Arneodo, N. Decoster, P. Kestener, and S. G. Roux, *Advances in Imaging and Electron Physics*, **126**, 1 (2003).
[68] P. Kestener and A. Arneodo, Phys. Rev. Lett. **91**, 194501 (2003); in *Proceedings of the 4th Pacific Symposium on Flow Visualization and Image Processing*, edited by J. Prenel and Y. Bailly (2003), to appear.
[69] P. Kestener, Ph.D. thesis, University of Bordeaux I, 2003.
[70] S. Chen, G. D. Doolen, R. H. Kraichnan, and Z. S. She, Phys. Fluids A **5**, 458 (1992).
[71] J. Molenaar, J. Herweijer, and W. Van de Water, Phys. Rev. E **52**, 496 (1995).
[72] G. Pedrizzetti, E. A. Novikov, and A. A. Praskovsky, Phys. Rev. E **53**, 475 (1996).
[73] L. P. Wang, S. Chen, J. G. Brasseur, and J. C. Wyngaard, J. Fluid Mech. **309**, 113 (1996).
[74] I. Hosokawa, S. Oide, and K. Yamamoto, Phys. Rev. Lett. **77**, 4548 (1996).
[75] A. Bershadskii, T. Nakano, D. Fukayama, and T. Gotoh, Eur. Phys. J. B **18**, 95 (2000).
[76] K. J. Falconer and T. C. O'Neil, Proc. R. Soc. Lond. A **452**, 1433 (1996).
[77] P. Kestener and A. Arneodo, "Generalizing the wavelet-based multifractal formalism to vector-valued random fields: application to turbulent velocity and vorticity 3D numerical data", Phys. Rev. Lett. (2004), to appear.
[78] G. H. Golub and C. V. Loan, *Matrix Computations*, 2nd ed. (John Hopkins University Press, Baltimore, 1989).
[79] We recall the relationship $h = \alpha - d$, between the Hölder exponent h and the singularity exponent α generally obtained by box-counting techniques ($D(\alpha - d) = f(\alpha)$) [20,63,71].
[80] B. Audit, E. Bacry, J. F. Muzy, and A. Arneodo, IEEE Trans. Info. Theory **48**, 2938 (2002).
[81] L. Chevillard, B. Castaing, and E. Lévêque, "On the rapid increase of intermittency in the near-dissipation range of fully developed turbulence", preprint (2003), cond-mat/0311409.
[82] L. Chevillard, S. G. Roux, E. Lévêque, N. Mordant, J. F. Pinton, and A. Arneodo, Phys. Rev. Lett. **91**, 214502 (2003).
[83] L. Chevillard, Ph.D. thesis, University of Bordeaux I, 2004.
[84] B. Castaing, Y. Gagne, and M. Marchand, Physica D **68**, 387 (1993).
[85] Y. Malécot, C. Auriault, H. Kahalerras, Y. Gagne, O. Chanal, B. Chabaud, and B. Castaing, Eur. Phys. J. B **16**, 549 (2000).
[86] O. Chanal, B. Chabaud, B. Castaing, and B. Hebral, Eur. Phys. J. B **17**, 309 (2000).
[87] A. N. Kolmogorov, C. R. Acad. Sci. USSR **30**, 301 (1941).
[88] W. Van de Water and J. Herweijer, Bull. Am. Phys. Soc. **41**, 1782 (1996).
[89] R. Camussi and R. Benzi, Phys. Fluids **9**, 257 (1997).
[90] O. N. Boratov and R. B. Pelz, Phys. Fluids **9**, 1400 (1997).
[91] S. Grossmann, D. Lohse, and A. Reeh, Phys. Fluids **9**, 3817 (1997).
[92] R. A. Antonia and B. R. Pearson, Europhys. Lett. **40**, 123 (1997).

[93] B. Dhruva, Y. Tsuji, and K. R. Sreenivasan, Phys. Rev. E **56**, R4928 (1997).
[94] S. Chen, K. R. Sreenivasan, M. Nelkin, and N. Cao, Phys. Rev. Lett. **79**, 2253 (1997).
[95] *Universality in Chaos*, edited by P. Cvitanovic (Hilger, Bristol, 1984).
[96] *Chaos*, edited by B. L. Hao (World Scientific, Singapore, 1984).
[97] H. G. Schuster, *Deterministic Chaos* (Physik Verlag, Weimheim, 1984).
[98] P. Bergé, Y. Pomeau, and C. Vidal, *Order within Chaos* (Wiley, New York, 1986).
[99] A. N. Kolmogorov, J. Fluid Mech. **13**, 82 (1962).
[100] A. M. Obukhov, J. Fluid Mech. **13**, 77 (1962).
[101] I. Hosokawa and K. Yamamoto, Phys. Fluids A **4**, 457 (1992).
[102] A. A. Praskovsky, Phys. Fluids A **4**, 2589 (1992).
[103] S. T. Thoroddsen and C. W. Van Atta, Phys. Fluids A **4**, 2592 (1992).
[104] G. Stolovitzky, P. Kailasnath, and K. R. Sreenivasan, Phys. Rev. Lett. **69**, 1178 (1992).
[105] J. O'Neil and C. Meneveau, Phys. Fluids A **5**, 158 (1993).
[106] G. Stolovitzky and K. R. Sreenivasan, Rev. Mod. Phys. **66**, 229 (1994).
[107] Y. Gagne, M. Marchand, and B. Castaing, J. Phys. II France **4**, 1 (1994).
[108] A. A. Praskovsky and S. Oncley, Europhys. Lett. **28**, 635 (1994).
[109] R. Benzi, S. Ciliberto, C. Baudet, and G. R. Chavarria, Physica D **80**, 385 (1995).
[110] S. T. Thoroddsen, Phys. Fluids **7**, 691 (1995).
[111] S. Chen, G. D. Doolen, R. H. Kraichnan, and L. P. Wang, Phys. Rev. Lett. **74**, 1755 (1995).
[112] V. Borue and S. A. Orszag, Phys. Rev. E **53**, R21 (1996).
[113] R. Benzi, R. Struglia, and R. Tripiccione, Phys. Rev. E **53**, R5565 (1996).
[114] S. G. Roux, Ph.D. thesis, University of Aix-Marseille II, 1996.
[115] E. D. Siggia, J. Fluid Mech. **107**, 375 (1981).
[116] R. Kerr, J. Fluid Mech. **153**, 31 (1985).
[117] S. Chen, K. R. Sreenivasan, and M. Nelkin, Phys. Rev. Lett. **79**, 1253 (1997).
[118] V. S. L'vov and I. Procaccia, Phys. Fluids **8**, 2565 (1996).
[119] G. He, S. Chen, R. H. Kraichnan, R. Zhang, and Y. Zhou, Phys. Rev. Lett. **81**, 4636 (1998).
[120] I. Arad, B. Dhruva, S. Kurien, V. S. L'vov, I. Procaccia, and K. R. Sreenivasan, Phys. Rev. Lett. **81**, 5330 (1998).
[121] I. Arad, V. S. L'vov, and I. Procaccia, Phys. Rev. E **59**, 6753 (1999).
[122] M. Nelkin, Phys. Fluids **11**, 2202 (1999).
[123] M. E. Brachet, Fluid Dyn. Research **8**, 1 (1991).
[124] Z. S. She, E. Jackson, and S. A. Orszag, Nature **344**, 226 (1990); Proc. Roy. Soc. London **434**, 101 (1991).
[125] A. Vincent and M. Meneguzzi, J. Fluid Mech. **225**, 1 (1991); **258**, 245 (1994).
[126] O. Metais and M. Lesieur, J. Fluid Mech. **239**, 157 (1992).
[127] J. Jimenez, A. A. Wray, P. G. Saffman, and R. S. Rogallo, J. Fluid Mech. **255**, 65 (1993).
[128] M. Tanaka and S. Kida, Phys. Fluids A **5**, 2079 (1993).
[129] A. Pumir, Phys. Fluids **6**, 2071 (1993).
[130] R. Camussi and G. Guj, J. Fluid Mech. **348**, 177 (1997).
[131] M. Farge, G. Pellegrino, and K. Schneider, Phys. Rev. Lett. **87**, 054501 (2001).
[132] A. Douady, Y. Couder, and M. E. Brachet, Phys. Rev. Lett. **67**, 983 (1991).
[133] S. Fauve, C. Laroche, and B. Castaing, J. Phys. II France **3**, 271 (1993).
[134] P. Abry, S. Fauve, P. Flandrin, and C. Laroche, J. Phys. II France **4**, 725 (1994).
[135] N. K.-R. Kevlahan, and J. C. Vassilicos Proc. R. Soc. Lond. A. **447**, 341 (1994).
[136] O. Cadot, S. Douady, and Y. Couder, Phys. Fluids **7**, 630 (1995).
[137] E. Villermaux, B. Sixou, and Y. Gagne, Phys. Fluids **7**, 2008 (1995).
[138] F. Belin, J. Maurer, P. Tabeling, and H. Willaime, J. Phys. II France **6**, 1 (1996).
[139] B. Dernoncourt, J. F. Pinton, and S. Fauve, Physica D **117**, 181 (1998).
[140] C. Baudet, O. Michel, and W. J. Williams, Physica D **128**, 1 (1999).
[141] F. Nicolleau, and J. C. Vassilicos Phil. Trans. R. Soc. Lond. A **357**, 2439 (1999).
[142] Y. Cuypers, A. Maurel, and P. Petitjeans, Phys. Rev. Lett. **91**, 194502 (2003).